01 Jan 2022

Effect of Spallation on Oxidation Kinetics of Heat-Resistant Cr–ni Austenitic Steels on Air and Combustion Atmosphere

Simon N. Lekakh
Missouri University of Science and Technology, lekakhs@mst.edu

Oleg Neroslavsky

Mei Li

Larry Godlewski

et. al. For a complete list of authors, see https://scholarsmine.mst.edu/matsci_eng_facwork/2904

Recommended Citation

S. N. Lekakh et al., "Effect of Spallation on Oxidation Kinetics of Heat-Resistant Cr–ni Austenitic Steels on Air and Combustion Atmosphere," *Oxidation of Metals*, Springer, Jan 2022.
The definitive version is available at https://doi.org/10.1007/s11085-022-10139-x

Oxidation of Metals (2023) 99:79–99
https://doi.org/10.1007/s11085-022-10139-x

ORIGINAL PAPER

Effect of Spallation on Oxidation Kinetics of Heat-Resistant Cr–Ni Austenitic Steels on Air and Combustion Atmosphere

Simon N. Lekakh[1] · Oleg Neroslavsky[2] · Mei Li[3] · Larry Godlewski[3] · Wenhui Zhu[3]

Received: 5 August 2022 / Revised: 27 October 2022 / Accepted: 4 November 2022 /
Published online: 21 November 2022

Abstract

Thin-walled castings made from Cr–Ni austenitic steels offer a combination of light weight of a near-net component with significant high temperature corrosion protection by forming a surface oxide layer. However, above critical service conditions (temperature, atmosphere, thermal cycling), oxidized surface can result in intensive surface degradation due to scale spallation. Scale spallation can decrease the wall thickness which could be detrimental to the in-service life of thin-walled castings. Experiments and stochastic simulations of spallation assisted oxidation were performed with three cast austenitic heat-resistant steels having different Cr–Ni concentrations at temperatures between 900 and 1000 ℃ on air and water vapor containing combustion atmosphere. The recorded specimen and spalled scale weight together with SEM and TEM analysis were used to predict the oxidation constant to form adherent layer and spallation intensity. Three oxidation modes, including oxidation controlled by diffusion with forming a strongly adherent to steel surface multi-layered scale, spallation assisted oxidation, and oxidation with additional partial vaporization of scale components in the water vapor environment were distinguished. It was revealed that the Cr and Ni concentrations moved temperature boundaries between these surface degradation mechanisms depending on the exposed oxidation environment. Our approach is aimed to alleviate an appropriate alloy selection for service conditions.

Keywords Austenitic steel · Oxidation · Spallation

✉ Simon N. Lekakh
lekakhs@mst.edu

[1] Missouri University of Science and Technology, Rolla, MO 65409, USA

[2] West Long Island LP, Long Island City, NY 11101, USA

[3] Research and Innovation Center, Ford Motor Company, Dearborn, MI 48124, USA

Introduction

Oxidation of Cr-Ni steels often results in the formation of layered surface oxide which are distinguishable by their composition [1–3]. Several oxides layers could be formed simultaneously or sequentially at different growth rates. Typically, the inner layer consists of dense Cr-bearing oxide, while the outer, formed with Fe-based oxides, is significantly weaker. In addition, in Cr–Ni steels, alloyed by Al, an alumina oxide film can form directly at the metal/scale boundary. This scale potentially protects the oxidized surfaces during long periods of near steady-state service exposures below some critical temperature, which is typically between 700 and 900 ℃ for heat-resistant austenitic steels [4]. During these temperature exposures, scale growth is followed by a near parabolic decline because it is controlled by element diffusion through the oxide layer.

It has been established that experimentally obtained oxidation kinetics in Cr–Ni austenitic steels below 700 °C well fit to a parabolic law; however, a significant departure from a parabolic law was observed in specific austenitic stainless steels exposed on air above 800 °C [5–9]. To fit the experimental results, a combination of linear and parabolic law was considered. For example, a weight gain at 400 °C in 316L stainless steel follows a parabolic law, while it deviates from a parabolic law for temperatures between 600 and 800 °C [10]. The several reasons for such deviations were discussed, including the different diffusion coefficients for of O, Cr, Fe, and Ni through the oxide films at different oxidation temperatures as well as changing thermodynamic stability of formed oxides, which altered the final multi-layered oxide structure. All these considerations assume that the formed oxide layer has a dense structure and is well adherent to the metal matrix, which typically takes place at relatively moderate oxidation temperatures in a static thermal condition without thermal cycling.

However, when increasing the temperature in addition to exposure a more aggressive atmosphere, such as in a water vapor combustion gas mixture, and imposing external thermo-mechanical stress can initiate the formation of defects within the scale [11, 12]. The oxide layers can experience external stress due to mechanical loading and also internal stress resulted by the specific volume difference between the oxide and base alloy, as well as the difference in thermal expansion. Depending on the net stress and temperature, the oxide scale can undergo deformation and finally fracture in multiple manners. This can enable a free path for gas oxidant directly to the scale/metal interface, which can lead to intensive oxidation. In such conditions, the resulting oxidation rate does not decline with time but rather is high and stable without deceleration. It is difficult to formalize such a complicated process using only governing equations for gas and metal ion diffusion for multi-layered structures formed on Cr–Ni austenitic steels with several moving reaction boundaries. This is primarily due to uncertainties about how to describe these mechanisms and dynamics of forming defectiveness. The local interface detachment of the oxide layer can expose a new surface to develop newly formed oxides. The scale detachment leads to an increase in the local rate of oxidation and intensifies the diffusion flux of metal ion outward of and oxygen

cation inward during the oxidation process [13]. The surface oxidation and oxide spallation behavior of austenitic and ferritic heat-resistant cast steels were investigated in isothermal and cyclic conditions. It was shown that ferritic steel appeared to be more resistant to oxide spallation than the austenitic alloys which was related to aggregation of interface defects [14]. The appearance of cracks and pores in scale structures also promote the diffusion rate of Cr, Fe, and O. The mechanisms of breakaway oxidation in chromia forming steel were described in [15]. Therefore, oxidation kinetics can deviate from the parabolic law at 800 °C in the studied austenitic steel [10] and experimentally measured weight gain during oxidation cannot be directly used to calculate an "actual" oxidation constant. The term "actual" refers to the oxidation kinetics of the newly formed oxide.

Adhesion of the oxide layer to the steel substrate depends on various parameters; among them are the thickness of the scale, its growth rate, the stress state, the interfacial energy, and the elastic properties of the oxide [16, 17]. The several local (micro-scale) approaches were used to describe the possible mechanisms of blistering, including nucleation, growth, coalescence, shrinkage, and finally spallation from oxidized surface. Specifically, a concept of critical strain in the scale needed for formed oxide layer spallation was suggested [18]. Another approach used a comprehensive operational parameter w_o that summarizes in a multi-level treatment of all contributing factors, e.g., physical defect size, interface roughness, scale thickness, Young's modulus, fracture toughness, etc., that influence failure strain [19].

Considering the difficulty to quantitatively describe the oxidation process including spallation using micro-models, there have been several statistical macro-models suggested. For example, the effect of spallation and subsequent surface renovation on overall parabolic oxidation kinetics was considered in the spallation model (COSP) designed for cyclic oxidation [20]. A deterministic interfacial cyclic oxidation spallation model (DICOSM) treated loss of individual oxide segments as events occurring after every thermal cycle [21]. Another model was developed using an analytical approach [22] which was based on the DICOSM model and fitted to two parameters, including a parabolic rate constant and a discrete oxide spallation probability at each cycle (between 0 and 1). These models were used to quantify oxidation and spallation during frequent thermal cycling, such as gas turbine components, when probability of spallation event was linked to a thermal cycle frequency.

In our work [23], in order to simulate the time-dependent process of oxidation with scale spallation, it was assumed that while growth of the residual oxide layer follows the parabolic equation, the stochastic process of spallation occurs in the oxide layer. A suggested stochastic model, which considers a topology of spalled scale and spallation intensity, was suggested. Here, it is important to mention that topological parameters used in the suggested stochastic model could be experimentally measured. Briefly, it was assumed that this stochastic process is a compound Poisson process. Jump size distribution is given by the table which expresses the time frequency of the diameters of spallation spots. After each simulated spallation event, the thickness of the oxide layer is adjusted and the decrease in the remaining layer leads to the accelerated oxidation. To make the simulation results more realistic, the model also uses several topological restrictions, such as K-ratio of spalled layer thickness (l) to scale thickness (L). Because the typical scale structure in Cr–Ni

austenitic steels consisted of an external and dense internal layers, cracking and spallation often occurs at the boundary between these layers, a K value could be estimated from the cross-sectional analysis.

The stochastic model [23] has the potential to predict three types of kinetics of spallation assisted oxidation, depending on variations in the spallation topology and spallation event frequency (Fig. 1). The first type of kinetics, which follows the parabolic law, represent the case of limited spallation with almost adherent scale to the specimen surface (Fig. 1a). There also is a variety of oxidation kinetics which could be described as a combination of near linear and parabolic trends for different spalled diameter distribution and spallation frequency (Fig. 1b). In another more extreme case, when there is a large spallation location and in the presence of high spallation frequency, there exist a short initial period during which a growth of adherent scale can lead to an intensive spallation condition that virtually removes all newly formed scales from the interface, leaving only a tiny adherent layer (Fig. 1c).

This study was motivated by the development of cast alloys for thin-walled exhaust systems to support the development of more efficient combustion engines. Prediction of both processes, including surface oxidation and spallation is important in this application. To study these assumptions, 400 h duration tests were performed in the air and combustion gas atmospheres at moderate and extreme elevated temperatures. Specifically, the study was focused on experimental verification and simulation of the spallation assisted oxidation process in three cast heat-resistant austenitic steels, having different Cr–Ni concentrations.

Procedures

Experimental

Three heat-resistant Cr–Ni austenitic steels with different Cr and Ni concentrations were used in this study [4]. Cr promotes oxidation resistance when exposed to high temperature environments by forming chromia and more complex oxides in scale. Additions of N and Mn were used to help Ni to stabilize the austenite structure,

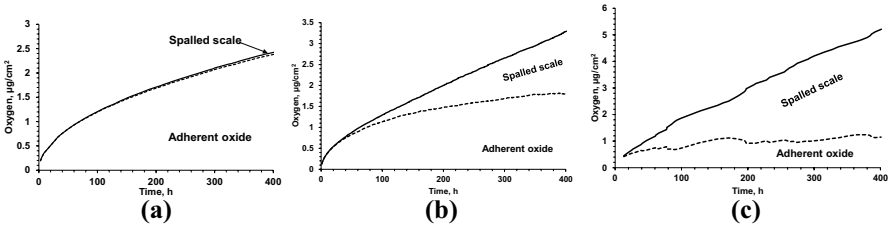

Fig. 1 Three types of predicted oxidation kinetics with a variation in spallation intensity: **a** oxidation with little spallation, **b** accelerated oxidation due to spallation, and **c** effect of intensive spallation on reformed oxide scale. Dashed line presents the amount of strongly adherent scale, solid line presents the total amount of oxygen reacted to metal, and area between these two lines presents the amount of oxygen in spalled scale [23]

Si was added to improve oxidation resistance by forming silica protection film on matrix/scale boundary, and Nb was added for creep resistance (Table 1). The studied steel had different amount of Cr and Ni and were referred to in the article as: economically alloyed steel (A), medium alloyed steel (B), and high alloyed steel (C). Grades of steels in these ranges are commonly considered for car exhaust systems.

The steel was melted in a 100 kg capacity induction furnace and poured into no-bake sand molds to produce 18 mm wall thickness plate castings. Samples were machined from plate castings into rectangular specimens 35 × 15x5 mm. Each sample was prepared using wet grinding with 60 grit silicon carbide, the surface quality was measured to have a Ra of 0.27 µm using 3D optical profiler (Nanovea, Model PS50 Micro Photonic Inc.). To prevent rusting prior to testing, the sample surfaces were preserved by immersion in ethanol and air dried. Static oxidation testing was performed in still air or a synthetic combustion atmosphere (15 vol.% CO_2, 2 vol.% O_2, 15 vol.% water vapor, N_2 balance.) and thermally exposed at 900 ℃, 950 ℃, and 1000 ℃ for a duration of 400 h. Prior to testing, the samples were put into thermally stabilized cylindrical alumina crucibles 50 mm tall, which had a 20 mm internal diameter, to collect the spalled scale during the exposure. The target test temperatures were defined to expose the samples to the upper working temperatures of exhaust components and test times were sufficient to simulate service conditions. Oxidation tests were interrupted after 50, 100, 200, and 300 h during the thermal exposure to measure: (1) the weight of specimens with adherent scale and (2) collected spalled scales formed during time step. Spalled scale was removed after each time step to decrease possible vaporization of Cr compounds. The total weight change was calculated from the weight change of the specimen with adherent scale and the collected spalled scale. One specimen was used for each thermal condition. 15% accuracy of measured total weight change was determined from a preliminary test of 3 specimens of steel B at 950 ℃ during 400 h on air; however, a large difference was observed in distribution between the adherent and spalled scale (up to 25%) because of complicated nature of spallation.

The spalled scale was evaluated using two techniques for chemical composition: ICP (Inductively Coupled Plasma) method to quantify the metallic elements and LECO combustion to measure the amount of oxygen which could be differ from calculated assuming stoichiometry. The total amount of oxygen consumed for oxidation was defined from the total weight change of specimen with collected spalled scale per unit area (mg/cm^2) and distributed into two parts: (1) oxygen in spalled scale, considering the weight of the scale and wt. % of oxygen measured from Leco analysis and (2) oxygen in adherent oxide layer as a difference between the total oxygen and the oxygen in spalled scale.

Table 1 Composition of studied austenitic steel (wt. %)

Steel	C	Si	Mn	Cr	Ni	Nb	N
A	0.3	1.5	1.0	20	10	2.0	0.2
B	0.41	1.6	1.8	22	11	1.5	0.1
C	0.41	1.2	1.9	26	13	1.7	0.1

SEM/EDX (Vega 3, Tecscan with Bruker spectrometer) analysis was performed on the oxidized surfaces to estimate the spallation geometry and to evaluate the cross section of the scale structure and steel structure. The specimens for TEM analysis were prepared using focused ion beam (FIB) on a Thermo Fisher Helios 650 Nanolab SEM/FIB. The Scanning TEM (STEM) imaging was carried out using a Thermo FisherTalos F200X STEM operated at 200 kV and equipped with an integrated energy dispersive.

X-ray spectrometer (EDS) with four silicon drift detectors.

Stochastic Simulation

The stochastic method suggested in our article [23] was used to simulate the process of oxidation with effects of geometrical parameters of scale spallation and frequency of spallation events. Briefly, it was assumed that the growth of the oxide layer follows the parabolic law while the stochastic process of spallation occurs within the oxide layer. It was assumed that this stochastic process is a compound Poisson process. Input into simulation includes a variable representing an actual oxidation constant and an intensity of spallation for experimentally determined topology of spalled scale as the distribution of spalled spot diameters. The measured weight change of specimens as well as the weight of spalled scale, were used to evaluate the spallation frequency and oxidation constants.

Experimental Results

Oxidation Tests

The total weight changes in three studied alloys during 400 h exposure to oxidation on air at 900 ℃, 950 ℃, and 1000 ℃ are shown in Fig. 2. In economical, low alloyed steel A, weight gain at lower temperatures follows a near parabolic trend; however, at higher temperatures, the weight gain accelerates with oxidation time. In a high alloyed steel C, weight gain was significantly less than in steel A, and primarily follows a near parabolic trend at all test temperatures. The medium alloyed steel B follows an intermediate trend in between these.

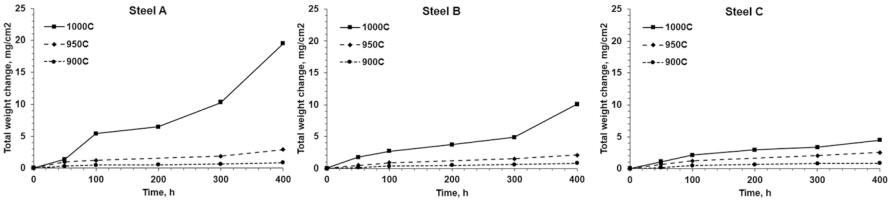

Fig. 2 Total weight change during high temperature oxidation of three studied steels at different temperatures on air

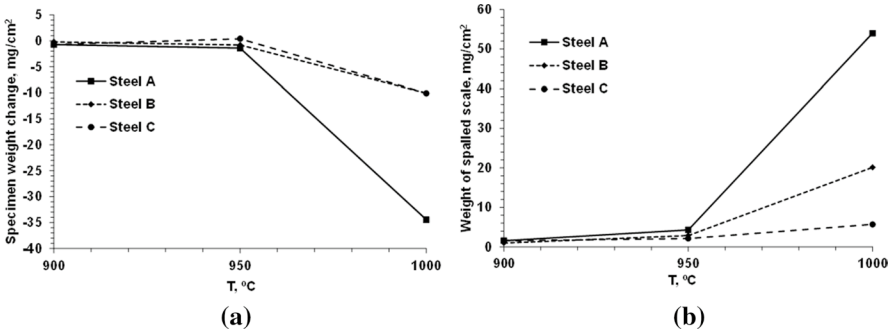

Fig. 3 Temperature effects on weight of specimen with adherent scale **a** and weight of spalled scale **b** in studied steels after 400 h holding on air

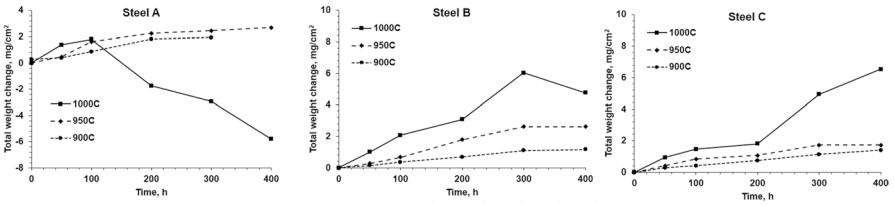

Fig. 4 Total weight change during high temperature oxidation of three studied steels at different temperatures in the combustion atmosphere

The effect of temperature on the weight change of specimen with adherent scale and the amount of collected spalled scale after 400 h hold time on air for all studied steels is shown in Fig. 3. When increasing the temperature above 950 ℃, significant amount of spallation occurred in alloyed steel A, while the oxidation rate and spallation in high Cr–Ni alloyed steel C was minimal and appeared to have a linear acceleration with temperature. The medium alloyed steel B showed an intermediate behavior with some increased spallation at 1000 ℃.

Similar tests were performed in water vapor containing combustion gas atmosphere; however, the results were significantly different from those observed on air. In steel A (Fig. 4, left), the total weight change continued to increase when holding time at temperatures lower than 950 ℃, but a weight loss was observed after 100 h oxidation when the test temperature was elevated to 1000 ℃. In steel B (Fig. 4, center), the weight gain increased at all test temperatures but decreased after 300 h at 1000 ℃. Only in high alloyed steel C, the weight gain increased when holding time at all test temperatures (Fig. 4, right).

The effect of temperature on the total weight gain and the amount of collected spalled scale after 400 h holding time in the combustion gas atmosphere for all studied steels is shown in Fig. 5a. Different trends were observed in the three studied steels: weight gain was observed in medium alloyed (steel B) and high alloyed (steel C) and weight loss was observed in the low alloyed steel A;

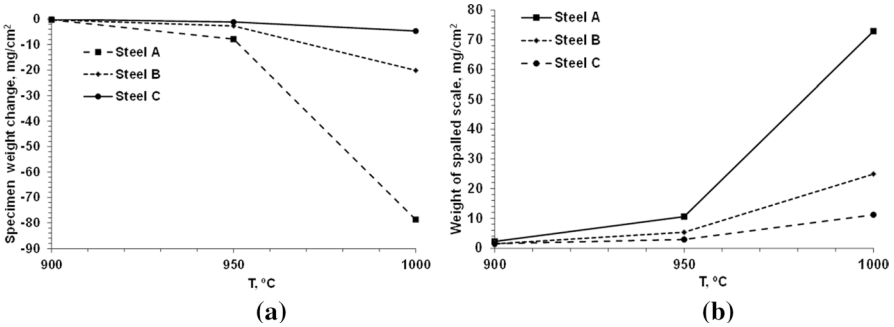

Fig. 5 Temperature effects on weight of specimen with adherent scale **a** and weight of spalled scale **b** in studied steels after 400 h holding in the combustion gas atmosphere

however, the weight of spalled scale significantly increased for elevated test temperatures in all test conditions (Fig. 5b).

Scale Structure

Scale structure was evaluated in the cross section and top surface view to quantify the spallation topology. Figure 6a illustrates a set of elemental maps for the cross section and Fig. 6b top view of air oxidized steel A tested at 950 ℃ during 400 h holding time. The multi-layered scale structure contains discontinuous silica rich interface, a dense chromite internal layer, and an external layer containing a mixture of Fe–Mn–Cr oxides. The location of a spalled site reveals a region of the inner oxide which is high in Cr (Fig. 6b).

Detailed TEM analysis was performed to obtain high resolution information characterizing the metal/scale interface for steel A (950 ℃ after 400 h in the air). Figure 7 summarized findings, indicating discontinuous, approximately 200 nm

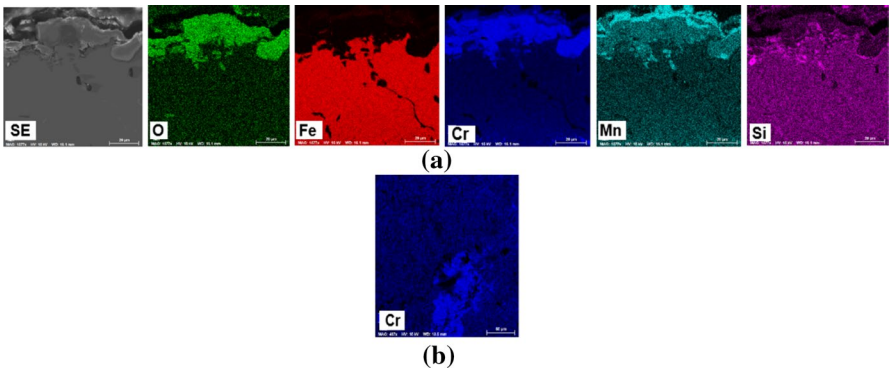

Fig. 6 Elemental map in cross-section **a** and Cr map from top view with line marked spalled area **b** of steel A oxidized at 950 ℃ during 400 h on air

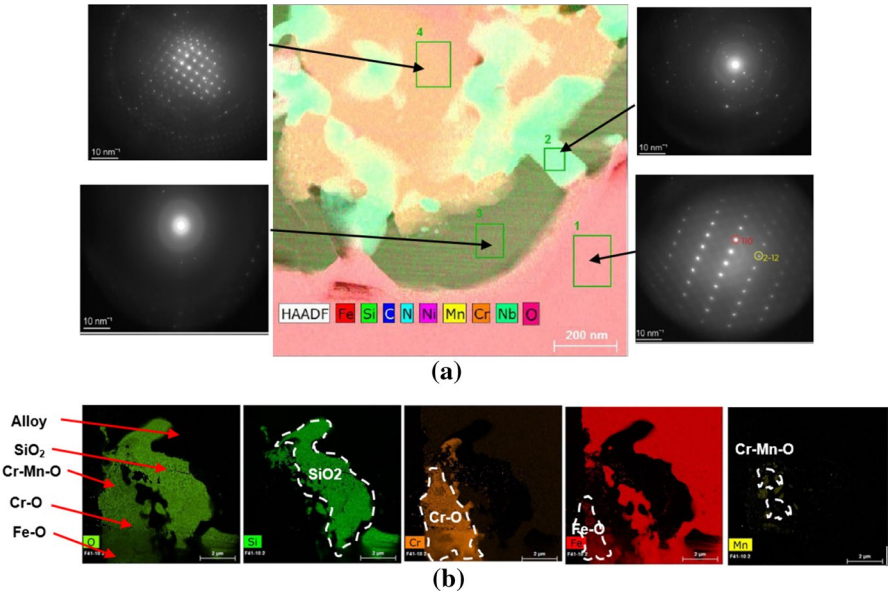

Fig. 7 TEM analysis of boundary between oxidized steel and scale for oxidation at 950 ℃ during 400 h on air steel *A* **a** and steel *B* **b**

thick amorphous silica film (region 3) on metal interface (region1), interrupted by partially oxidized nano-structured NbCN (region 2), and extended into dense solid solution type Cr–Mn oxides (region 4). Table 2 presents the local chemical compositions in these regions and indicates local Cr depletion from austenite to chromia into the scale.

Increasing the oxidation temperature and water vapor in the combustion atmosphere significantly influenced the topology of the adherent to the matrix and the detached oxides (Fig. 8 and Table 3). The scale has multiple defects (pores and cracks) with sporadically layered composition resulting in multiple spallation events. Pieces of the amorphous silica films randomly located near the boundary which contained austenite (point 1), followed by a chromia layer 2 with interface topology but also extended deep in scale. External regions contained a mixture of Fe, Mn, and Cr oxides (point 4 and 5) and small spots of complex Nb–Cr oxides were sporadically

Table 2 EDX analysis of regions shown in Fig. 7a (wt. %)

Region—phase	Fe	Si	C	N	Ni	Mn	Cr	Nb	O
1—Austenite	72	0.98	0.25	0.37	10.8	0.5	8.3	0.53	–
2—Nb–C–N–O	2.3	13.2	0.76	1.65	0.67	0.31	1.1	60.7	8.7
3—Amorphous SiO_2	5.0	48.9	0.46	0.9	0.9	0.3	0.8	0.8	39.4
4—(Cr,Mn)-oxide	1.6	0.32	0.43	0.4	0.55	21.3	50.5	0.8	19.7

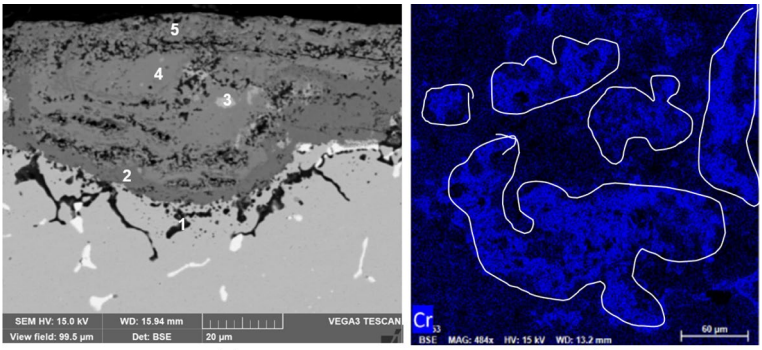

Fig. 8 Cross-section SEM image with points for EDX analysis **a** and Cr map from top view **b** of steel *A* oxidized at 1000 ℃ during 400 h in the combustion atmosphere

Table 3 EDX chemical analysis (wt. %) of scale in steel A oxidized at 1000 ℃ during 400 h in the combustion atmosphere (points from Fig. 8)

Point	O	Si	Cr	Mn	Fe	Ni	Nb
1	45	32	15	4	3	–	–
2	32	–	65	–	1	1	–
3	21	–	44	–	–	–	31
4	25	–	25	–	27	21	–
5	29	–	48	–	19	5	–

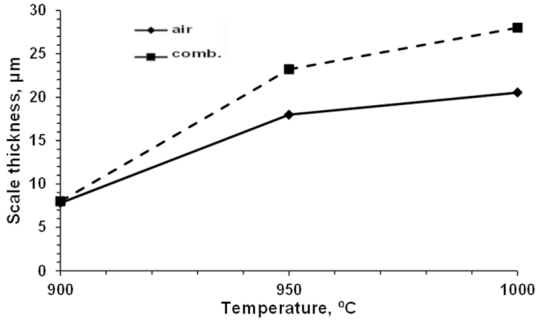

Fig. 9 Average thickness measured in 10 points scale and formed during 400 h oxidation tests of steel *A*

located within the scale. The top view indicated regions of detached scale (Fig. 8b) and the topology of spalled scale from elemental map was used as input in stochastic modeling of spallation assisted oxidation. Increasing the oxidation temperature and water vapor environment increased the thickness of residual adherent scale on steel A (Fig. 9).

The steel composition had a significant effect on the scale structure and thickness. For comparison, Fig. 10 and Fig. 11 present elemental maps of the cross section for both the medium and high Cr–Ni alloyed steels B and C, oxidized on air at 950 ℃ for a duration of 400 h. In both cases, more consistent amorphous silica film

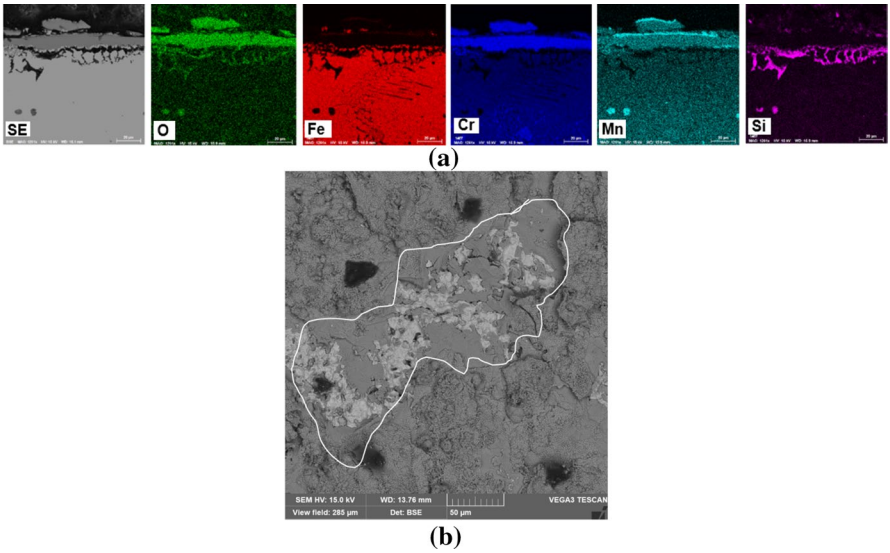

Fig. 10 Elemental map in cross section **a** and top view with line marked spalled area **b** of steel B oxidized at 950 ℃ during 400 h on air

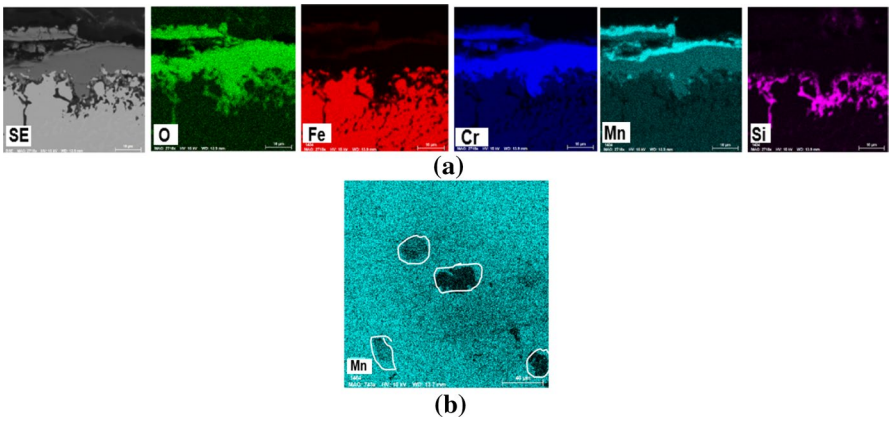

Fig. 11 Elemental map in cross section **a** and Mn map from top view with line marked spalled area **b** of steel C oxidized at 950 ℃ during 400 h on air

existed at the austenite/scale boundary as compared to alloy A, (Fig. 6), followed by several pure, relatively dense chromia layers that contained several lateral cracks. Each of the chromia layers were covered by a complex external Fe–Mn–Cr oxide, which indicated several spallation events occurred during the long oxidation exposure time. Steel C had a smaller (30–50 microns) diameter distribution of spalled spots which are well noticeable in the Mn map taken from top view (Fig. 11b).

Chemical composition of the spalled scale from all three steels (Table 4) verified that the detached layers mostly consisted of Fe–Mn–Cr oxides which indicated

Table 4 Chemical composition of metallic elements in spalled scale from ICP method (wt. %)

Steel	Si	Mn	Cr	Ni	Nb	Fe
A	1.8	1.1	10.7	10.2	1.5	75
B	1.9	2.0	10.5	11.5	0.9	73
C	1.8	2.3	12.3	10.6	0.9	72

that cracks and detachment mainly occur between the internal chromia layer and the defected external layer consisted of mixed oxides.

The experimental data collected during the study was used to simulate the amount of spallation assisted oxidation for each of the steels tested. This was done at elevated temperatures on air and water vapor environments containing combustion atmosphere.

Discussion

The external surfaces of exhaust manifolds are generally exposed on air, while the internal surfaces work in contact with hot water vapor/combustion gas atmospheres. The tests were performed on air and combustion atmosphere at temperatures above 900 ℃ to mimic severe service exposure of a gas exhaust system commonly used in energy efficient combustion engines. The results show that these conditions could be above a typical operation window when the growth of the dense oxide layer is controlled only by diffusion. Therefore, it is important to understand the effect of the gas atmosphere on oxidation kinetics above some critical temperature diapason when the spallation affected oxidation takes place. In this work, stochastic modeling of spallation assisted oxidation was implemented. This modeling used experimentally determined amounts of oxygen reacted to form adherent oxides and spalled scale. Two measurements were used—changing weight of a specimen with adherent scale and weight of spalled oxide. Additional information about topology of spalled spots was used to predict frequency of spallation and to calculate an "actual" oxidation constant to form an adherent scale.

Oxidation on Air

Figure 12 presents the weight of spalled scale in logarithmic scale after 400 h thermal exposure at different temperatures for the three studied steels. There was minimal spallation observed during the thermal exposure on air at 900 ℃ for all steels. However, as the temperature increased from 900 ℃ to 1000 ℃, the spallation intensity increased in order of magnitude. The higher alloying Cr–Ni levels in steel B and steel C appeared to significantly prevent spallation on air.

As shown in Table 4, a typical chemistry of the spalled scale indicated that it contained nearly half the amount of Cr as compared to the concentration in the steel matrix (Table 1). This suggests that buckling and detachment of the oxide skin mainly occurred within external oxide layers, consisting of complex Fe–Mn–Cr

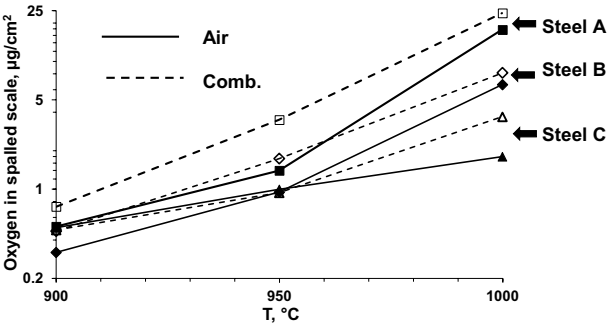

Fig. 12 Effect of test temperature and environment on weight of oxygen in spalled scale after 400 h oxidation tests

oxides (Fig. 7). Determined by combustion analysis an average oxygen concentration in spalled scale (33 wt. %) together with the spalled scale weight and the total weight gain were used to calculate the amount of oxygen in a spalled scale and in a strongly adherent internal oxide layer. The experimental oxygen data are represented in Fig. 13 by dots for oxygen in adherent oxide and triangles for the total oxygen content. The difference between these values presented oxygen in a spalled scale. This data were used to simulate the spallation assisted oxidation within the suggested stochastic model, and the results are shown by solid line for total oxygen and dashed line for the oxygen in the adherent oxide per unit of area for steel B oxidized on air at 900 ℃ (a), 950 ℃ (b), and 1000 ℃ (c). Increasing the test temperature from 900 ℃ to 1000 ℃ dramatically intensified oxidation rate (see different scale on *Y*-axes) and also increased the portion of oxygen within the spalled scale (area between solid and dashed lines). The calculated actual oxidation constant ($mg^2/cm^4/h$) increased from 2.0e-7 at 900 ℃ to 2.2e-5 at 1000 ℃. The spallation frequency also increased for the given test temperatures from 0.3 to 0.8 $1/h/cm^2$.

Using a similar approach, all experimental data presented in Fig. 1–4 were processed to determine parameters of spallation assisted oxidation, including the actual oxidation constant and spallation intensity. Below, the key findings are presented

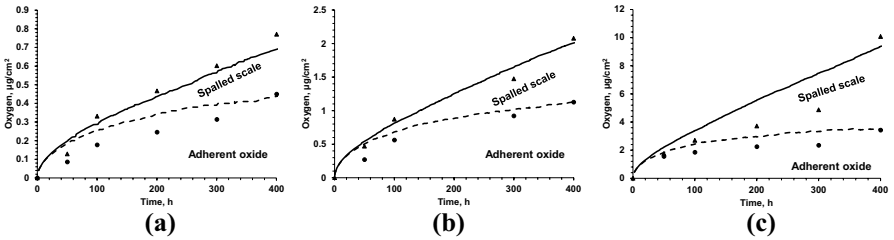

Fig. 13 Simulated spallation assisted oxidation on air of steel B at 900 ℃ **a**, 950 ℃ **b**, and 1000 ℃ **c**. Oxygen in adherent scale shown by circular marker and dashed line, total oxygen shown by triangular marker and solid line

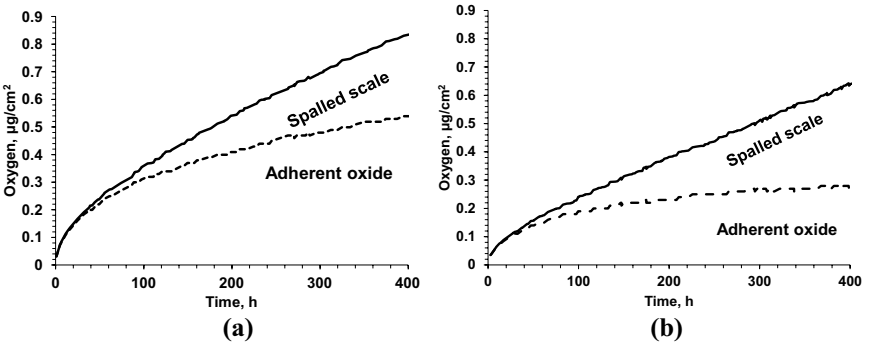

Fig. 14 Simulated spallation assisted oxidation on air of steel A **a** and steel C **b** at 900 ℃ **b**. Oxygen in adherent scale shown by dashed line and total oxygen by solid line

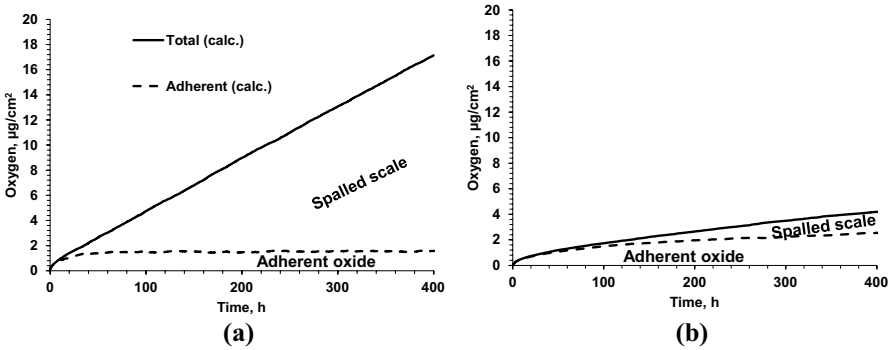

Fig. 15 Simulated spallation assisted oxidation on air of steel A **a** and steel C **b** at 1000 ℃ **a**. Oxygen in adherent scale shown by dashed line and total oxygen by solid line

to highlight the significant effect of the steel composition and oxidation condition (temperature and atmosphere) on parameters of spallation assisted oxidation. The level of Cr/Ni alloying had a minimal effect on oxidation kinetics on air at 900 ℃. Figure 14 illustrates oxidation kinetics in low (20/10) and high (26/13) Cr/Ni levels in steel A and steel C. The calculated actual oxidation constants ($mg^2/cm^4/h$) for all conditions were 3.0E-7 (steel A), 2.0E-7 (steel B), and 1.2E-7 (steel C).

However, the difference in oxidation kinetics in studied steels significantly increased at high oxidation temperature on air and was mainly attributed to the changes in the spallation intensity. At 1000 ℃ the total amount of oxygen in steel A, was 4 times higher than in the steel C, and after 400 h exposure the main factor was the difference which occurred by spallation (Fig. 15). In steel A, there was intensive spallation which suppressed the growth of the adherent layer shortly after the initial period. In contrast, the high alloyed steel C, showed near parabolic growth of the adherent layer at 1000 ℃. The amount of spallation in steel B indicated an intermediate behavior between these two steels (Fig. 12). These results indicated the significance to analyze both the spalled and adherent oxides because looking at only

the specimen weight gain or thickness of remaining adherent oxide does not fully characterize the oxidation processes for the tested conditions.

Effect of Oxidizing Atmosphere

Contained water combustion atmosphere intensified the amount of spallation as compared to on air for all temperatures (Fig. 12). At the lower temperature (900 ℃) in steel B, water vapor increased both rates: actual oxidation constant from 2.0E-7 to 6.0E-7 $mg^2/cm^4/h$ and spallation frequency ($1/h/cm^2$) from 0.3 to 0.4. The simulated curves for oxygen in spallation scale and the adherent layer are shown in Fig. 16. It is evident that the growth of the adherent layer still shows near parabolic behavior for both atmospheres. Similar trends were observed in low Cr–Ni steel A and high Cr–Ni steel at lowest test temperature.

The reaction kinetics completely changed when the oxidation test was performed for the low and medium alloyed steel A and steel B at the higher temperature. They had orders of magnitude higher measured weight of the spalled scale; however, a decrease in the total weight of a specimen plus collected spalled scale was also observed. There is only one conceivable explanation of the total weight loss of the system which consisted of both specimen and spalled scale after oxidation test: this loss is due to intensive vaporization. The mechanism of vaporization is linked to formation of chromium hydroxide from reaction of chromia with water vapor at high temperatures [24]. Such compound has a relatively high partial gas phase pressure which could be vaporized during long exposure time at high temperature while being exposed to a water vapor environment. Figure 17a illustrates experimental data for steel A, performed at 1000 ℃ in a combustion atmosphere. The specimen loss of weight was near 80 mg/cm^2 during the 400 h test, which is approximately the same amount as was gained by spalled scale; however, the total weight change in the system was negative.

In this work, we used stochastic modeling of spallation assisted oxidation. This modeling used the experimentally determined amount of oxygen reacted to form adherent oxides and spalled scale. Two measurements were used—changing

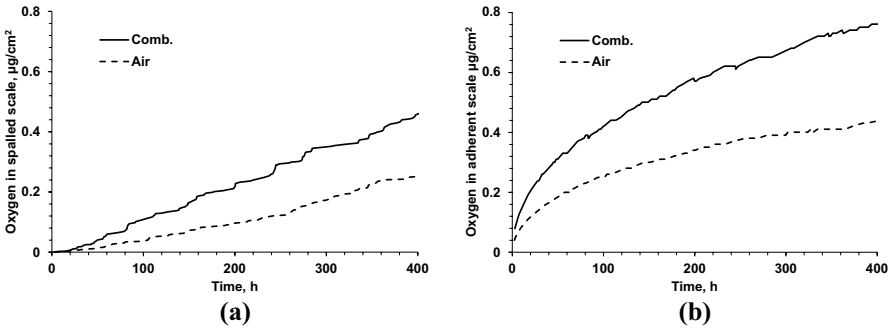

Fig. 16 Kinetics of spallation **a** and actual oxidation **b** in steel B oxidized at air and combustion gas atmosphere at 900 ℃

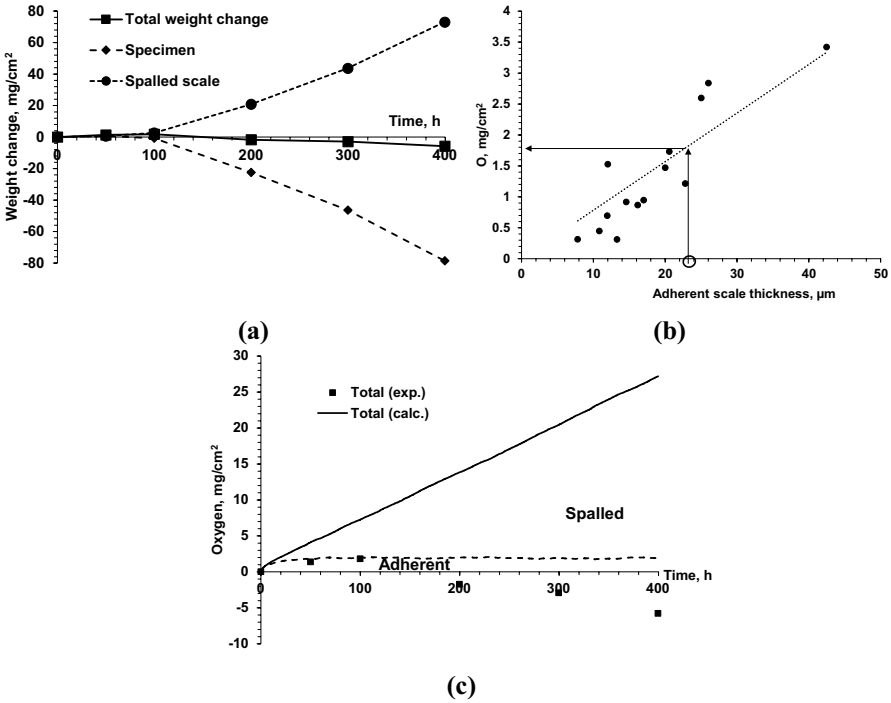

Fig. 17 Illustration of assessing vaporization to adjust stochastic modeling spallation assisted oxidation of steel A at 1000 ℃ in water vapor containing combustion atmosphere: **a** experimentally measured weight change, **b** determination of oxygen in adherent scale based on SEM measured scale thickness, and **c** simulated adjusted kinetics

weight of a specimen with adherent scale and weight of spalled oxide. Additional information about topology of spalled spots was used to predict a frequency of spallation and also the "actual oxidation constant" to form an adherent scale was simulated. This methodology allowed one to simulate experimental results and to determine these parameters for moderate oxidation conditions.

However, data from Fig. 17 illustrated that a combination of three factors (low Cr/Ni alloying level, high temperature and water vapor) potentially initiated active vaporization in addition to form adherent and spalled scale. In addition, collected from thermo-gravimetrical analysis two values (weight of specimen with adherent scale and spalled scale weight) were not enough to calculate three processes. Three mechanisms (actual parabolic oxidation with forming adherent scale, scale spallation, and vaporization) were present during high temperature oxidation in water contained environment and minimum one additional experimental parameter is needed to simulate such processes with a stochastic model. Because weight or volume of vaporized phases were not determined from experiment, an indirect method was used to estimate the vaporization by adjustment of weight of adherent scale from it thickness. Because the spalled scale has low Cr and it was collected after each time step, it could be assumed that a minimal

effect of vaporization on measured weight of spalled scale occurred, and the primary vaporization loss was from the adherent oxidation to the specimen Cr-rich layer. To quantify the amount of oxygen in adherent scale, a conversion of the SEM measured residual scale thickness to oxygen in adherent scale was determined in this study. Figure 17b illustrates the experimental results for the tests where vaporization had a minimal effect (solid markers) and approximation line for SEM measured thickness and oxygen which resides in the adherent layer from weight data. Using this approximation, SEM measured thickness for steel A at 1000 ℃ exposed in the combustion atmosphere (circle) was converted to the amount of oxygen.

The experimental thickness of adherent layer correlated to the amount of total oxygen in adherent layer obtained from thermo-gravimetrical analysis. However, there was a large amount of scatter observed due to the uncertainty related to determination of density of defected scale and multi-phase structure. The weight change presented the 3D volume averaging while SEM thickness results were obtained from several one-dimensional measurements. Scale brittleness is one more factor increasing data scattering. Therefore, it could be concluded that for such severe oxidation conditions, thermo-gravimetrical analysis can provide a more consistent data as compared to the data from sectioning and scale thickness measurements. In this work, measurement of adherent scale thickness was used to roughly estimate all these processes and special experimental methods may be required in future. An adjustment on vaporization spallation assisted oxidation for these test conditions are shown in Fig. 17c.

Such adjustments were needed only for higher temperature tests in the combustion atmosphere when the total weight losses were observed. For all other test conditions, tight correlations were observed between the predictions from the stochastic model and experimentally measured weight changes after 400 h. For such condition, these did not need a correction due to Cr vaporization (Fig. 18).

The summarized spallation assisted oxidation parameters for all test conditions are shown in Fig. 19. A suggested methodology enabled us to clearly identify two

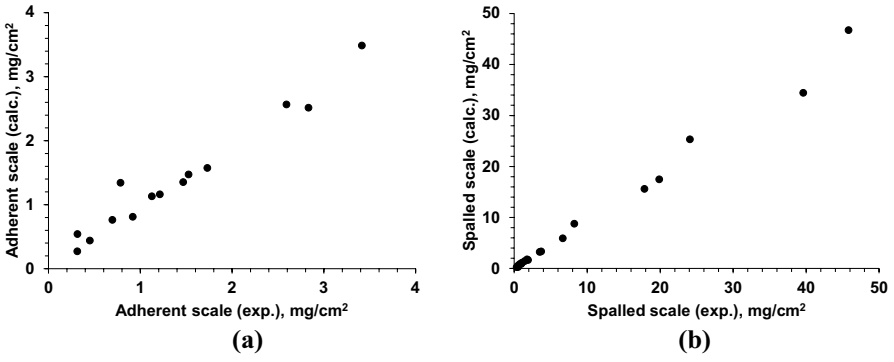

Fig. 18 Correlations between predicted from stochastic model of spallation assisted oxidation and experimentally determined oxygen in adherent **a** and spalled **b** scale for all test conditions where vaporization was not influenced

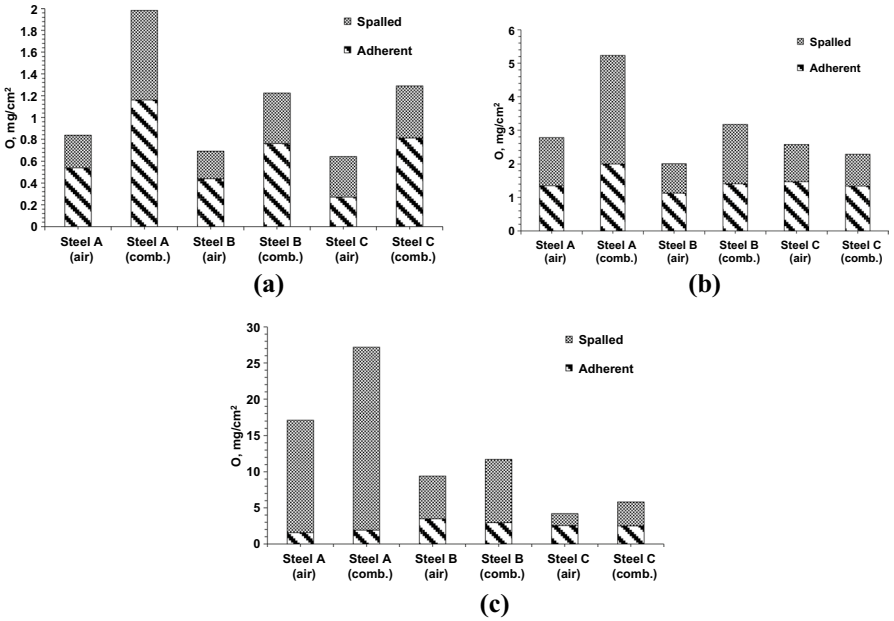

Fig. 19 Comparison of the amount of oxygen in adherent layer and spalled scale for studied steels after 400 h oxidation on air and combustion atmosphere at 900 ℃ **a**, 950 ℃ **b**, and 1000 ℃ **c**

processes: actual oxidation with formation of an adherent layer and the intensity of the spallation. The oxygen amount was used for this characterization, while these data could be recalculated in scale thickness.

Figure 20 shows the calculated values for the actual oxidation constants for adherent scale *vs* reciprocated absolute temperature (Arrhenius plot). It supports the conclusion that Cr–Ni alloying level has a stronger protection effect at higher

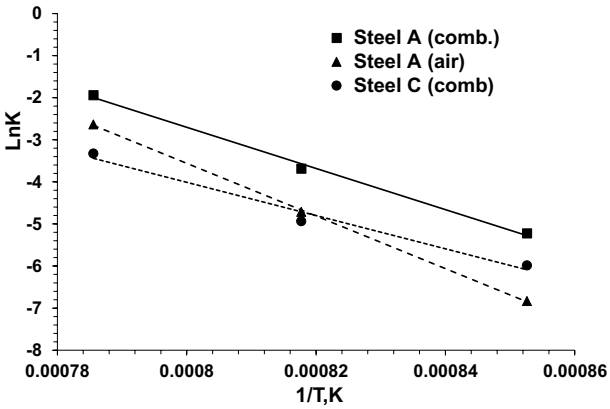

Fig. 20 Arrhenius plot for oxidation constant defined from spallation assisted stochastic simulation for steel *A* and steel *C* oxidized in different atmospheres

temperatures and especially in a water vapor environment. However, significantly larger values of the activation energy (> 400 kJ/mol) were determined from this plot for all studied conditions when compared to the results for a typical activation energy for pure diffusion-controlled oxidation (200–280 kJ/mol). This indicated a mutual effect of multiple processes during the studied high temperature exposures, which included the intensification of the adherent layer defectiveness by thermal stress and vaporization. Multi-layered scale structure contains oxides having different coefficients of thermal expansion. In addition, there is a significant difference in thermal expansion of oxides and austenitic steel. These processes have their own activation energy and influence on the calculated activation energy of forming the adherent layer during the spallation assisted process.

A stochastic model, used in this work, considers topology of spalled scale and spallation intensity. The model allows to calculate and to specify different degradation processes occurred during high temperature oxidation of studies austenitic steel. Based on experimental study and stochastic simulation results, the schematic of different surface degradation processes taking place in heat-resistant Cr–Ni austenitic steels was suggested for different Cr–Ni alloying levels (Fig. 21). The general sequence of oxidation processes with increasing temperature includes diffusion-controlled formation of well adherent scale (stage 1), spallation assisted oxidation (stage 2), and finally intensive oxidation with spallation and partial Cr-oxide vaporization (stage 3). For different working conditions, stage 1 could be recommended for extremely long lifetime because it is governed by the declining parabolic law. Stage 2 could be accepted for a component with medium time exposure to harsh environments. Stage 3, occurs only during peak temperature and short time conditions. The temperature window for these stages depends upon the type of environments and alloy compositions. Specifically, in studied steels additionally alloyed by Si, TEM study indicated that amorphous silica film was formed during oxidation on air at 950 ℃ and below (Fig. 7). This silica film could help Cr oxide to suppress diffusion of oxygen into the matrix. However, both the increase in the oxidation temperature and water vapor significantly influenced the topology of the adherent to the matrix oxides (Fig. 8). Pieces of amorphous silica films were randomly located near the metal matrix/scale interface. Examples of approximate temperatures for these working stages are shown for Steel A oxidized on air and water vapor containing combustion gas

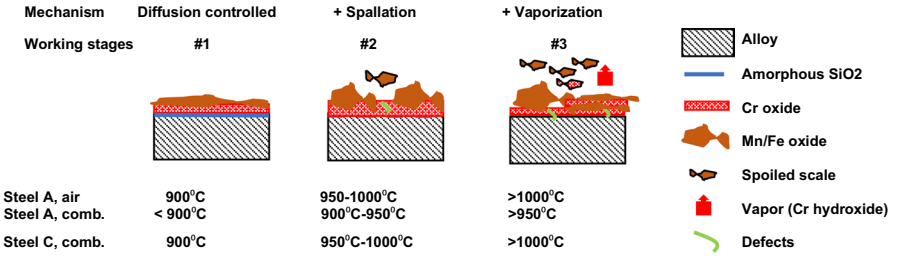

Fig. 21 Schematic of temperature- and atmosphere-dependent mechanisms of surface degradation of Cr–Ni heat-resistant steels below and above critical oxidation conditions

atmosphere in comparison with high Cr–Ni alloyed steel C. Such recommendation could be used for alloy design for specific working conditions.

Conclusions

An experimental study of high temperature oxidation on air and combustion gas, containing water vapor, was performed for three cast heat-resistant steels with varying Cr–Ni concentrations. For studied critical conditions, spallation assisted oxidation was simulated using a stochastic approach. The following assessment has been concluded:

- Scale spallation was present for all temperatures between 900 ℃ and 1000 ℃, in both air and combustion environments for all three heat-resistant austenitic steels;
- At 900 ℃, the steel composition showed minor effects during the thermal exposure on air, while less alloyed by Cr–Ni steel was more prone to spallation assisted oxidation in the combustion atmosphere. It was found that the actual oxidation constant and spallation intensity were higher when compared to the other steels;
- While being thermally exposed on air, at 950 ℃, it appeared to intensify the spallation for all steels and this process dominated at 1000 ℃, when major oxidation products were detached from steel surface;
- Both high and medium Cr–Ni alloying steels, had a significant advantage to prevent spallation at maximum test temperatures on air and combustion atmospheres;
- The surface degradation process was determined for different working conditions with establishing temperature boundaries for steels with varying Cr/Ni concentrations

The authors are hoping that the results might aid in appropriate alloy selection for service conditions.

Acknowledgments Great thanks to Dr. Laura Bartlett and Dr. Ron O'Malley for supporting research, PhD student Richard Osei for SEM analysis and undergrad student Caelen Johnson for experimental work.

Author Contributions SNL conceptualized and designed the experiment, ON performed simulations, SNL and LG analyzed experimental data, WZ performed TEM study, ML commented on previous versions of the manuscript and approved the fnal manuscript.

Funding This research was supported by the US Department of Energy's Office of Energy Efficiency and Renewable Energy (EERE) under the Award Number DE-EE0008458.

Declarations

Competing interests The authors declare no competing interests.

References

1. R. Pillai, A. Chyrkin, and W. J. Quadakkers, *Oxidation of Metals* **96**, 2021 (385).
2. R. Osei, S. Lekakh, and R. O'Malley, *Metallurgical and Materials Transactions B* **52B**, 2021 (393).
3. Ling Liu, et al., *Materials* **15**, 2022 (3515).
4. High-Temperature Characteristics of Stainless Steels, American Iron Steel Institute, A Designer's Handbook, Series 9004 (2011).
5. F. Pérez, et al., *Surface and Coating Technology* **108**, 1998 (127).
6. S. Wang, et al., *Corrosion Science* **72**, 2013 (64).
7. N. Karimi, et al., *Applied Surface Science* **254**, 2008 (2298).
8. G. Wood, *Corrosion Science* **2**, 1962 (173).
9. H. Li, et al., *Journal of Alloys Compound* **686**, 2016 (326).
10. Xi. Huang, et al., *Materials Research Express* **7**, 2020 066517.
11. M. Schutze, *Materials Science and Technology* **4**, 1988 (407).
12. W. Quadakkers, J. Żurek, and M. Hänsel, *JOM* **7**, 2009 (44).
13. J. Robertson and M. Manning, *Materials Science and Technology* **6**, 1990 (81).
14. S. Baleix, G. Bernhart, and P. Lours, *Material Science Engineering A* **327**, 2002 (155).
15. H. Evans, A. Donaldson, and T. Gilmour, *Oxidation of Metals* **52**, 1999 (379).
16. S. R. Pillai, et al., *Oxidation of Metals* **49**, 1998 (509).
17. F. H. Stott, G. C. Wood, and J. Stringert, *Oxidation of Metals* **44**, 1995 (113).
18. M. Schutze, *Oxidation of Metals* **44**, 1995 (29).
19. M. Schutze, P. Tortorelli, and I. Wright, *Oxidation of Metals* **73**, 2010 (389).
20. C. Lowell, et al., *Oxidation of Metals* **36**, 1991 (81).
21. J. L. Smialek, *Acta Materialia* **51**, 2003 (469).
22. D. Poquillon and D. Monceau, *Oxidation of Metals* **59**, 2003 (409).
23. S. Lekakh, et al., *Oxidation of Metals* **98**, 2022 (239).
24. H. Asteman, J. Svensson, and L. Johanssona, *Journal of the Electrochemical Society* **151**, 2004 (141).